Applied Physics Letters

RESEARCH ARTICLE | OCTOBER 01 2025

Enhancement of spin–orbit torque in sputtered BiSb-based perpendicular magnetic tunnel junctions for neuromorphic computing applications

S. Wu ; G. J. Lim ; F. N. Tan ; T. L. Jin ; C. C. I. Ang ; E. K. Koh ; S. H. Lee; K. J. Cheng ; W. S. Lew

Appl. Phys. Lett. 127, 132407 (2025)
https://doi.org/10.1063/5.0275455

AIP Publishing

Applied Physics Letters ARTICLE pubs.aip.org/aip/apl

Enhancement of spin–orbit torque in sputtered BiSb-based perpendicular magnetic tunnel junctions for neuromorphic computing applications

Cite as: Appl. Phys. Lett. **127**, 132407 (2025); doi: 10.1063/5.0275455
Submitted: 13 April 2025 · Accepted: 5 September 2025 ·
Published Online: 1 October 2025

S. Wu, G. J. Lim, F. N. Tan, T. L. Jin, C. C. I. Ang, E. K. Koh, S. H. Lee, K. J. Cheng, and W. S. Lew[a)]

AFFILIATIONS

School of Physical and Mathematical Sciences, Nanyang Technological University, 21 Nanyang Link, Singapore 637371, Singapore

[a)]Author to whom correspondence should be addressed: wensiang@ntu.edu.sg

ABSTRACT

Topological insulators offer unique properties for generating high spin–orbit torque (SOT), promising to revolutionize magnetoresistive random-access memory with a low power consumption. In this work, BiSb is integrated into perpendicular magnetic tunnel junctions (pMTJs) to enable efficient SOT switching. By optimizing the BiSb thickness and introducing a Ta buffer layer, a threefold enhancement in damping-like SOT efficiency and a 60% reduction in switching current are achieved compared to the BiSb-free sample. X-ray diffraction measurements confirm the improved crystalline quality with increasing BiSb thickness, contributing to the enhanced spin current generation. The fabricated BiSb-pMTJs exhibit key neuromorphic functionalities, including gradual long-term potentiation/depression and sigmoidal resistance modulation under pulsed current. Utilizing these features, a three-layer artificial neural network is implemented based on experimentally extracted device behavior, achieving over 90% accuracy in handwritten digit recognition.

Magnetoresistive random-access memory (MRAM) is regarded as a reliable nonvolatile emerging memory technology due to its long data retention and robust endurance.[1] The functionality of MRAM relies on magnetic tunnel junction (MTJ) structures, which store data in parallel or anti-parallel magnetization states of ferromagnetic (FM) layers, thereby exploiting tunneling magnetoresistance (TMR) for binary data representation.[2–5] Recent advances in MRAM technology have shifted toward spin–orbit torque (SOT) mechanisms to induce magnetization switching, presenting a compelling alternative to the conventional spin-transfer torque (STT) methods.[6–9] SOT exploits the spin–orbit coupling (SOC) in certain materials, where an applied charge current generates a transverse spin current, exerting torque on the adjacent FM layers without the need for the current to pass through the insulating barrier of the MTJ. This mechanism enhances switching efficiency, reduces energy consumption, and mitigates device degradation.[10–13] Conventional heavy metals such as Pt, Ta, and W have been widely used as spin current sources due to their strong spin–orbit coupling. However, their spin Hall angles are typically limited to values below ∼0.3, which limits the achievable reduction in switching current density and power consumption.[14–16] To address this constraint, topological insulators (TIs) have emerged as promising alternatives, offering highly efficient spin–charge conversion enabled by their characteristic electronic structure comprising an insulating bulk and spin-momentum-locked surface states.[17–21] Recent studies have reported that TI materials such as Bi_2Se_3 and $(Bi_{1-x}Sb_x)_2Te_3$ can deliver significantly enhanced SOT efficiencies, typically in the range of ∼0.8–1.5, thereby outperforming conventional heavy metals in spin current generation capability.[17,22] Among TIs, bismuth antimonide (BiSb) stands out due to its small bulk bandgap (∼20 meV), high electrical conductivity, and the coexistence of multiple Dirac surface states that enhance spin current generation.[23,24] However, the integration of TIs into spintronic devices faces several challenges. First, most demonstrations rely on epitaxial growth on lattice-matched substrates such as GaAs or Al_2O_3, which are incompatible with CMOS processes.[17,22] Second, the crystalline quality and interfacial properties of TIs degrade significantly during standard fabrication steps, limiting their practical adoption in large-scale memory architectures.[25] Third, most existing TI-based SOT devices are configured with in-plane magnetic anisotropy, which offers lower thermal stability and packing density compared to perpendicular magnetic tunnel junctions (pMTJs).[26–28]

Meanwhile, spintronic devices, particularly MTJs have attracted increasing attention for neuromorphic computing applications. Owing to their non-volatility, scalability, and current-driven switching dynamics, MTJs have been explored not only as memory elements but also as functional components in artificial neural networks (ANNs). Specifically, spintronic implementations of synapses and neurons have been demonstrated through mechanisms such as domain wall motion and spin–orbit torque-induced magnetization switching. These approaches enable tunable conductance and nonlinear transfer characteristics, including sigmoidal activation and spiking behavior, which are essential for hardware-based ANN inference and training.[29–31] These developments underscore the potential of MTJ-based spintronic platforms for building efficient, integrated, and energy-conscious neuromorphic systems.

In this work, we explore the integration of BiSb into pMTJ stacks using sputtering to enhance SOT efficiency. By optimizing the BiSb thickness and introducing a Ta buffer layer, we demonstrate a threefold increase in damping-like SOT efficiency and a 60% reduction in switching current compared to control devices without BiSb. X-ray diffraction (XRD) analysis reveals an improvement in crystalline quality with increasing BiSb thickness, which contributes to enhanced spin transparency and more efficient spin current generation at the interface. Importantly, the entire device is fabricated using industrially viable magnetron sputtering on thermally oxidized Si substrates, ensuring compatibility with back-end-of-line (BEOL) processing. Beyond memory applications, we further extend the functionality of BiSb-based pMTJs to neuromorphic computing. Modern computing systems face energy bottlenecks due to the separation of memory and logic units (the von Neumann bottleneck), especially in AI workloads involving large-scale matrix operations. Neuromorphic computing seeks to address this by employing memory elements that directly emulate the behavior of biological neurons and synapses.[32–34] In this context, we show that BiSb-pMTJs can mimic both synaptic weight modulation via long-term potentiation/depression (LTP/LTD) and sigmoidal neuron activation behavior through current-induced nonlinear switching. Using experimentally extracted device characteristics, we construct an artificial neural network (ANN) for handwritten digit recognition and achieve recognition accuracy of over 90%, validating the potential of these devices for energy-efficient, in-memory computing. These results demonstrate that sputtered BiSb is not only a scalable and CMOS-compatible spin current source but also a versatile platform for multifunctional spintronic applications integrating memory, logic, and neuromorphic computing.

The TI-MTJ stacks of $Bi_{0.85}Sb_{0.15}$ (40 nm)/Ta (3 nm)/CoFeB (1.4 nm)/MgO (1.5 nm)/CoFeB (1.6 nm)/Ta (1 nm)/[Co (0.6 nm)/Pt (0.6 nm)]$_6$/Co (0.6 nm)/Ru (0.5 nm)/Co (0.6 nm)/[Pt (0.6 nm)/Co (0.6 nm)]$_6$/Ta (3 nm)/Ru (3 nm)/Ta (3 nm) were deposited on thermally oxidized Si substrates by using a magnetron sputtering system at room temperature with a base pressure of 5×10^{-8} Torr. The thickness of each layer was controlled based on pre-calibrated sputtering rates obtained under fixed DC or RF power, Ar gas flow rate, working pressure, and sputtering time. The film thicknesses were measured using a Park NX10 atomic force microscope (AFM) operated in non-contact mode, and the deposition rates were calculated accordingly to determine the sputtering duration for each layer. The TI-MTJ devices were fabricated using photolithography, electron beam lithography (EBL), and Ar ion milling steps. Initially, an AR-N4340 negative-tone resist was utilized to pattern the TI underlayer, followed by etching of all layers using Ar ion milling and subsequent removal of the photoresist with acetone. Subsequently, MTJ pillars with circular shapes and diameters of 5 μm were patterned using electron beam lithography with an ma-N 2403 negative-tone resist and etched down to the MgO layer. A layer of 40 nm thick HfO_x was then sputtered to electrically isolate the top and bottom contacts of the tunnel junctions. Top electrodes were patterned using a photolithography step with AZ5214 positive-tone photoresist, followed by a 60 nm thick Ta layer deposition. Another photolithography and Ar ion milling step was performed to define and open the bottom electrodes, which succeeded by sputtering another 60 nm thick Ta layer. Finally, the fully patterned TI-MTJ devices were annealed at 260 °C for 30 min in a vacuum.

The magnetic properties of the TI-MTJ stack were measured using the vibrating sample magnetometer (VSM). The magnetic properties of the Hall bar devices were determined through electrical characterization via anomalous Hall effect (AHE) measurements. The SOT efficiency was determined by measuring the harmonic Hall voltages using a Keithley 6221 AC source and a 7265 Dual-Phase DSP Lock-In Amplifier.[35] The SOT switching in the 3-terminal TI-MTJ devices was measured using a Keithley 2400 source meter to apply the current and measure the resistance and a LakeShore electromagnet to provide the bias magnetic field. All these measurements were conducted at room temperature.

Figure 1(a) shows the schematic of the BiSb/Ta/CoFeB/MgO/Ta thin film stack. Figure 1(b) shows magnetic hysteresis (M–H_z) loops of the thin films with the BiSb thicknesses varying from 10 to 50 nm by sweeping the magnetic field (H_z) along the out-of-plane direction. The hysteresis loops with the square shape indicate the presence of PMA. As shown in Fig. 1(c), the coercivity (H_c) increases with BiSb thickness, ranging from 35 to 145 Oe. The inset illustrates the variation of root mean square roughness (R_q) as a function of BiSb thickness, showing a progressive increase with thickness (three-dimensional AFM images of films with different BiSb thicknesses are provided in supplementary material S1). This increase in R_q is closely linked to the observed changes in H_c. The enhanced roughness introduces additional pinning sites for magnetic domain walls. These pinning sites impede domain wall motion, thereby increasing the magnetic field required for magnetization reversal. As a result, the observed enhancement in H_c with BiSb thickness can be attributed to the increased domain wall pinning effect induced by the rougher interface. In-plane hysteresis measurements show that the effective anisotropy field H_k slightly increases with BiSb thickness, confirming that PMA is preserved (see supplementary material S2). Interlayers such as Ru and Ti were employed in previous research,[17,22,36] whereas, in this work, we have explored the use of Ta as another alternative interlayer material. As shown in Fig. 1(d), the 3 nm Ta interlayer is thick enough for PMA to manifest and serves as a buffer to prevent the exchange interaction between BiSb and CoFeB and to block the diffusion of elements during annealing, which could otherwise degrade the topological surface states. However, as the Ta layer decreased below 2 nm, we observed a significant reduction in PMA. This effect became even more pronounced when the Ta layer was further reduced to 1 nm, at which point PMA was completely absent, undermining the required film properties. This underscores the critical balance required, while a thinner Ta layer could theoretically improve spin current transmission, excessively thin layers compromise the magnetic stability necessary for the effective

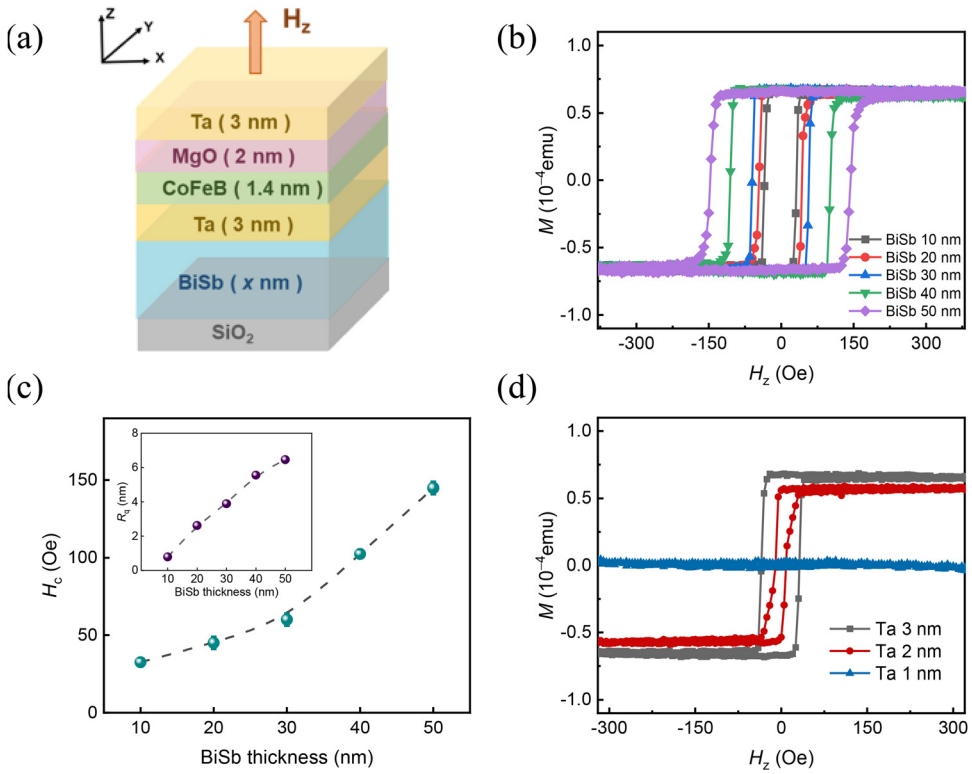

FIG. 1. (a) Schematic illustration of the BiSb/Ta/CoFeB/MgO/Ta film. (b) Out-of-plane magnetic hysteresis loops of the size of 1 cm × 1 cm BiSb (x nm)/Ta (3 nm)/CoFeB (1.4 nm)/MgO (2 nm)/Ta (3 nm) stack films with varying BiSb thicknesses. (c) The coercivity H_c as a function of BiSb thickness. The inset depicts the variation of root mean square roughness R_q with BiSb thickness. (d) Out-of-plane magnetic hysteresis loops of the size of 1 cm × 1 cm BiSb (10 nm)/Ta (x nm)/CoFeB (1.4 nm)/MgO (2 nm)/Ta (3 nm) stack films, demonstrating the influence of varying the thickness of the sandwiched Ta layer between BiSb and CoFeB on the magnetic properties.

PMA. Therefore, maintaining the Ta layer at 3 nm ensures an optimal trade-off, optimizing spin current efficiency while preserving the magnetic properties essential for reliable pMTJ functionality. Consequently, subsequent investigations were conducted with an intermediate Ta layer maintained at 3 nm thickness.

The BiSb (t_{BiSb})/Ta/CoFeB/MgO/Ta films, as well as a control sample without the BiSb layer ($t_{BiSb} = 0$ nm), were fabricated into 10 μm × 100 μm Hall cross device structures. Figure 2(a) shows the anomalous Hall resistance R_{AHE}–H_z loops of the measured Hall cross devices with varying BiSb thicknesses. Introducing the BiSb layer increased the interfacial roughness, leading to an impact on the H_c of the devices. Specifically, the devices without BiSb layers exhibited a smaller H_c compared to those with the BiSb layers. Subsequently, the current-induced magnetization switching (CIMS) for devices with different BiSb thicknesses was investigated, as shown in Fig. 2(b). The CIMS loops were measured using a series of DC pulses under an external in-plane magnetic field of −300 Oe. The pulse current was applied along the x-direction with a maximum magnitude of 30 mA and a duration of 5 ms. To evaluate the damping-like effective field efficiency (χ_{DL}) as a function of BiSb thickness, harmonic Hall voltage measurements were carried out. Figure 2(c) shows the dependence of the χ_{DL} and switching current I_{sw} on the BiSb thickness. The χ_{DL} shows an increase with increasing t_{BiSb}, saturating at around $(15.9 \pm 0.4) \times 10^{-10}$ Oe/(A/m^2) ($t_{BiSb} = 40$ nm), which is almost three times higher than the control sample ($t_{BiSb} = 0$ nm) of $(5.5 \pm 0.1) \times 10^{-10}$ Oe/(A/m^2). The average switching current for the 40 nm BiSb sample was 8 mA, approximately 60% lower than the control sample at 20 mA. The enhanced SOT efficiency in BiSb can be attributed to its large spin Hall angle and high electrical conductivity, which significantly improve charge-to-spin current conversion efficiency. BiSb's topological surface states enable spin-momentum locking, which facilitates robust spin current generation and efficient magnetization switching. Furthermore, as demonstrated by the x-ray diffraction (XRD) θ–2θ spectra in Fig. 2(d), increasing BiSb thickness enhances the crystalline quality, as evidenced by the increase in diffraction peak intensities without significant peak shifts, indicating stable lattice parameters (additional XRD θ–2θ spectra of BiSb heterostructures with varying thicknesses on thermally oxidized Si substrates over the broader $2\theta = 20°$–$80°$ range are provided in supplementary material S3). Although AFM results show increasing surface roughness with BiSb thickness, this roughness mainly reflects morphological evolution of the BiSb surface. The comparatively low R_a values confirm that the overall height variation remains modest (see supplementary material S1). The enhanced crystallinity observed in XRD is therefore identified as the dominant factor contributing to the improved SOT efficiency. Notably, the improvement in crystallinity saturates at $t_{BiSb} = 40$ nm, with negligible changes observed for $t_{BiSb} = 50$ nm, suggesting that further thickness increase does not lead to significant structural or

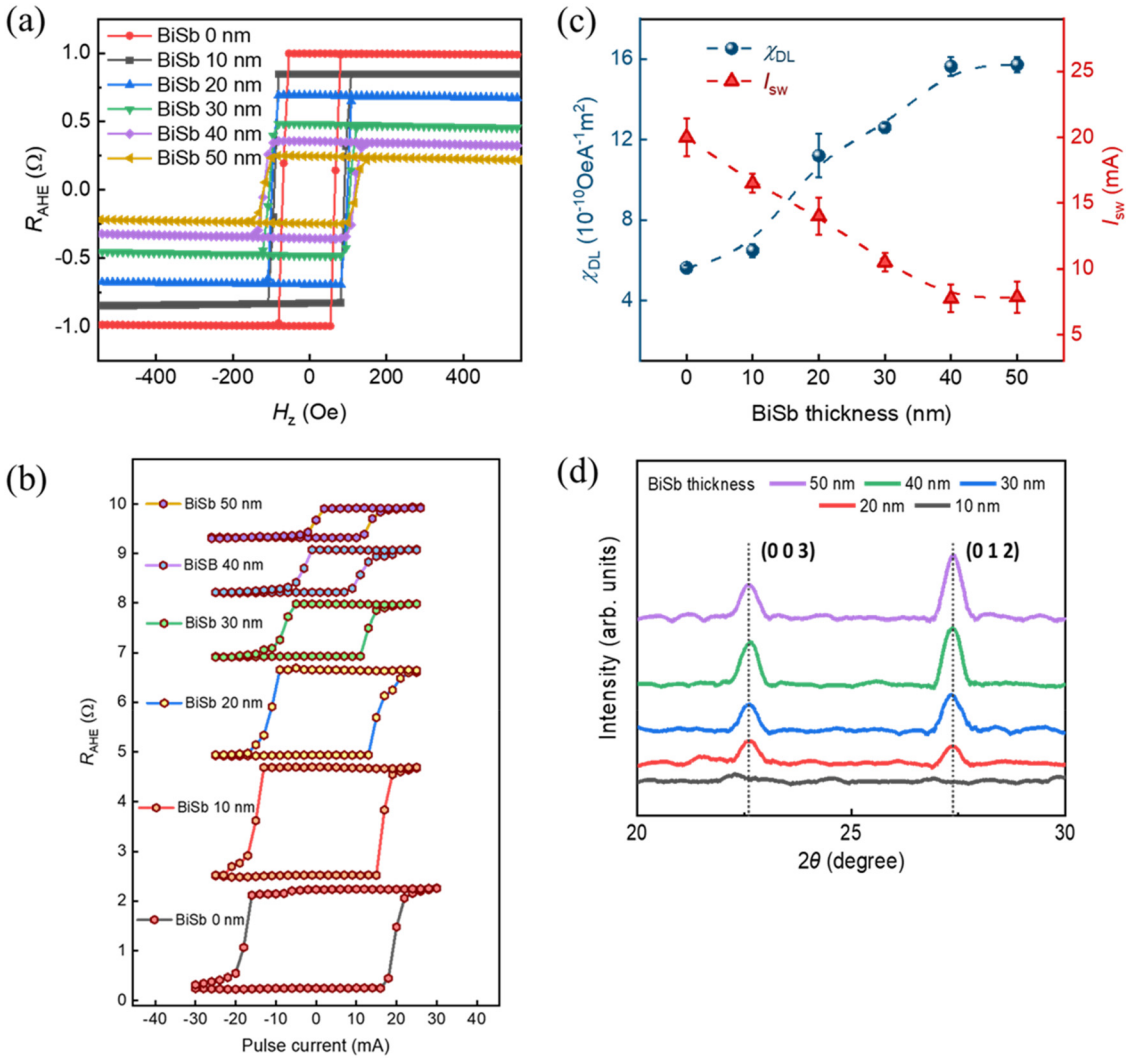

FIG. 2. (a) Anomalous Hall resistance loops measured in BiSb/Ta/CoFeB/MgO/Ta Hall cross devices with different BiSb thicknesses under an out-of-plane field. (b) Current-induced magnetization switching in devices with different BiSb thicknesses under an external in-plane magnetic field of −300 Oe. (c) The damping-like field SOT efficiency χ_{DL} and switching current I_{sw} as a function of BiSb thickness for the devices. (d) XRD θ–2θ spectra of BiSb heterostructures with different BiSb thicknesses in the range of $2\theta = 20°$–$30°$. The (003) and (012) diffraction peaks are indicated.

electronic improvements. This saturation in crystalline quality correlates with the plateau observed in χ_{DL}, indicating that optimal SOT efficiency is achieved at $t_{BiSb} = 40$ nm, making it the ideal thickness for maximizing spin–charge conversion while maintaining minimal energy dissipation. The Ta buffer layer thickness is fixed at 3 nm in all devices and functions primarily to preserve PMA and maintain a clean interface, rather than to serve as a variable spin current source. Control experiments varying Ta thickness from 3 to 5 nm at fixed BiSb thickness show negligible change in χ_{DL}, indicating a constant Ta contribution (see supplementary material S4). Therefore, subsequent investigations focus on BiSb with $t_{BiSb} = 40$ nm, highlighting the critical role of BiSb thickness engineering in optimizing charge-to-spin conversion efficiency and achieving efficient SOT-driven magnetization switching.

Figure 3(a) illustrates the out-of-plane magnetic hysteresis loops of BiSb-based MTJ films with the incorporation of a synthetic antiferromagnetic (SAF) structure. The SAF structure, comprising two $[Co/Pt]_6$ multilayers coupled antiferromagnetically, induces notable modifications in the magnetic behavior of the film. This effect is primarily attributed to the antiferromagnetic exchange coupling within the SAF, which stabilizes the magnetic orientation of the reference layer by counteracting thermal fluctuations and external magnetic field disturbances.[37] Figure 3(b) demonstrates a schematic overview of the layered structure within the BiSb-based perpendicular MTJ device. The schematic structure in Fig. 3(c) illustrates a 3-terminal SOT-driven TI-pMTJ device, where the 40 nm thick BiSb layer, optimized for enhanced SOT efficiency, serves as the SOT channel. The strong spin-momentum locking at the surface states of the BiSb layer generates

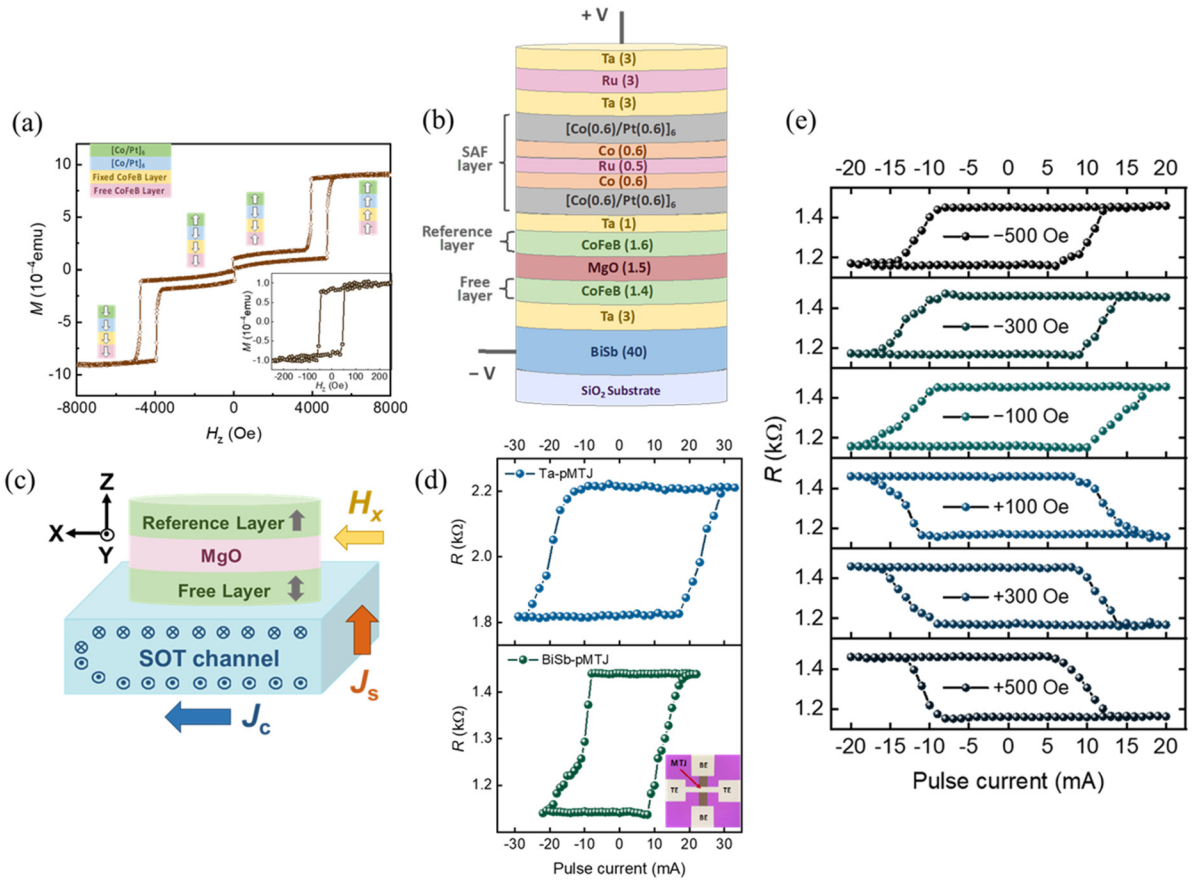

FIG. 3. (a) Out-of-plane magnetic hysteresis loops of the BiSb-based MTJ film with a synthetic antiferromagnetic (SAF) layer. The SAF structure comprises two antiferromagnetically coupled $[Co/Pt]_6$ multilayers. The minor hysteresis loops were measured under a small magnetic field. (b) Schematic of the sputtered BiSb-based perpendicular magnetic tunnel junction. (c) Schematic of a 3-terminal SOT-driven TI-pMTJ device. (d) Current-induced magnetization switching in pMTJ devices with and without a BiSb layer (Ta-based reference). The inset shows the optical micrograph of the patterned MTJ device with a diameter of 5 μm. (e) Current-induced magnetization switching in all-sputtered BiSb-pMTJ devices under different external in-plane magnetic fields.

spin-polarized currents, which exert torques on the magnetic moments of the free layer, facilitating magnetization switching. Subsequently, current-induced SOT switching was performed in the BiSb-based pMTJ device. Figure 3(d) shows current-induced magnetization switching in pMTJ devices with and without a BiSb layer (Ta-based reference). The inclusion of a BiSb layer significantly reduces the switching current, decreasing from 21 mA in the Ta-based reference device to 11 mA in the BiSb-based device, corresponding to a 48% reduction. The optical micrograph of the patterned MTJ device is shown in the inset, where the BiSb layer serves as the bottom electrode contact and the TI-MTJ pillar with a 5 μm diameter size is located at the intersection region between the bottom electrodes (BE) and top electrodes (TE). Here, we demonstrate a TI-pMTJ film fabricated entirely by magnetron sputtering on a Si/SiO_2 substrate, in contrast to conventional TI thin films, which are often single-crystalline and epitaxially grown on specific III–V semiconductor substrates like GaAs and Al_2O_3 using molecular beam epitaxy, making them unsuitable for mass production.[25] Figure 3(e) demonstrates the current-induced magnetization switching for the all-sputtered BiSb-pMTJ devices under different external in-plane magnetic fields. During operation, the 5 ms writing current pulses were applied in the BiSb channel to provide the SOT for magnetization switching of the bottom free CoFeB layer with an in-plane magnetic field. The magnetization state of the free CoFeB layer is subsequently read by measuring the resistance of the MTJ using a small DC reading current of 100 μA between the top and bottom electrodes. TMR curves measured as a function of out-of-plane magnetic field for different batches of BiSb-based pMTJ devices are provided in supplementary material S5. Moreover, current-induced magnetization switching in all-sputtered BiSb-based pMTJ devices with a BiSb thickness of 40 nm for various MTJ diameters (800 nm, 1 μm, 3 μm, and 5 μm) is presented in supplementary material S6. These results demonstrate stable TMR behavior across all MTJ devices, with the 800 nm diameter device exhibiting the highest TMR of 40%. The incorporation of a BiSb layer, leveraging its strong spin-momentum locking, significantly enhances SOT efficiency in pMTJ devices. The BiSb thickness of 40 nm is optimized to maximize spin current generation while minimizing the switching current, highlighting its critical role in advancing SOT-MTJ technology.

Following the demonstration of enhanced SOT in BiSb-pMTJ devices, their direct application in neuromorphic computing architectures is explored. As shown in Fig. 4(a), a three-layer artificial neural network (ANN) architecture is constructed for digit recognition tasks, comprising 784 input neurons (corresponding to 28×28 pixels of MNIST images), 300 hidden neurons with sigmoid activation functions, and 10 output neurons representing the classification outcomes.[38] The implementation leverages the multi-resistance states of BiSb-pMTJs to emulate both neuronal and synaptic functionalities. Figure 4(b) presents the resistance modulation behavior of a BiSb-pMTJ device as a function of pulse current amplitude. The resistance exhibits a nonlinear, S-shaped dependence, analogous to the sigmoid activation function commonly used in ANN models.[39] This behavior enables direct hardware implementation of analog neuronal activation using current-induced magnetization switching. The inset shows the full hysteresis loop of current-driven switching, confirming the device's robust switching capability. Figure 4(c) demonstrates synaptic plasticity through long-term potentiation (LTP) and long-term depression (LTD), achieved by applying a sequence of 40 current pulses with an amplitude of ± 10 mA. The normalized Hall resistance R_{xy} is gradually modulated in opposite directions for LTP and LTD, resembling the weight update mechanism in biological synapses. Both the experimental data (Exp_LTP and Exp_LTD) and their corresponding fits (Fit_LTP and Fit_LTD) show smooth, monotonic behavior, supporting reliable incremental programming suitable for hardware-based learning algorithms. Figure 4(d) presents the evolution of digit recognition accuracy using the MNIST dataset, comparing an ideal ANN with the one implemented using experimentally measured BiSb-pMTJ synaptic weights. Despite the nonidealities in resistance modulation, the BiSb-pMTJ-based ANN achieves over 90% classification accuracy, validating the potential of BiSb-pMTJs as spintronic synaptic devices for in-memory neuromorphic computing. These results highlight the feasibility of integrating BiSb-based spintronic devices for both synaptic and neuronal functions in future energy-efficient, scalable neuromorphic hardware systems.

In conclusion, we have demonstrated the integration of BiSb into perpendicular magnetic tunnel junctions using a CMOS-compatible sputtering process. By optimizing the BiSb thickness and incorporating

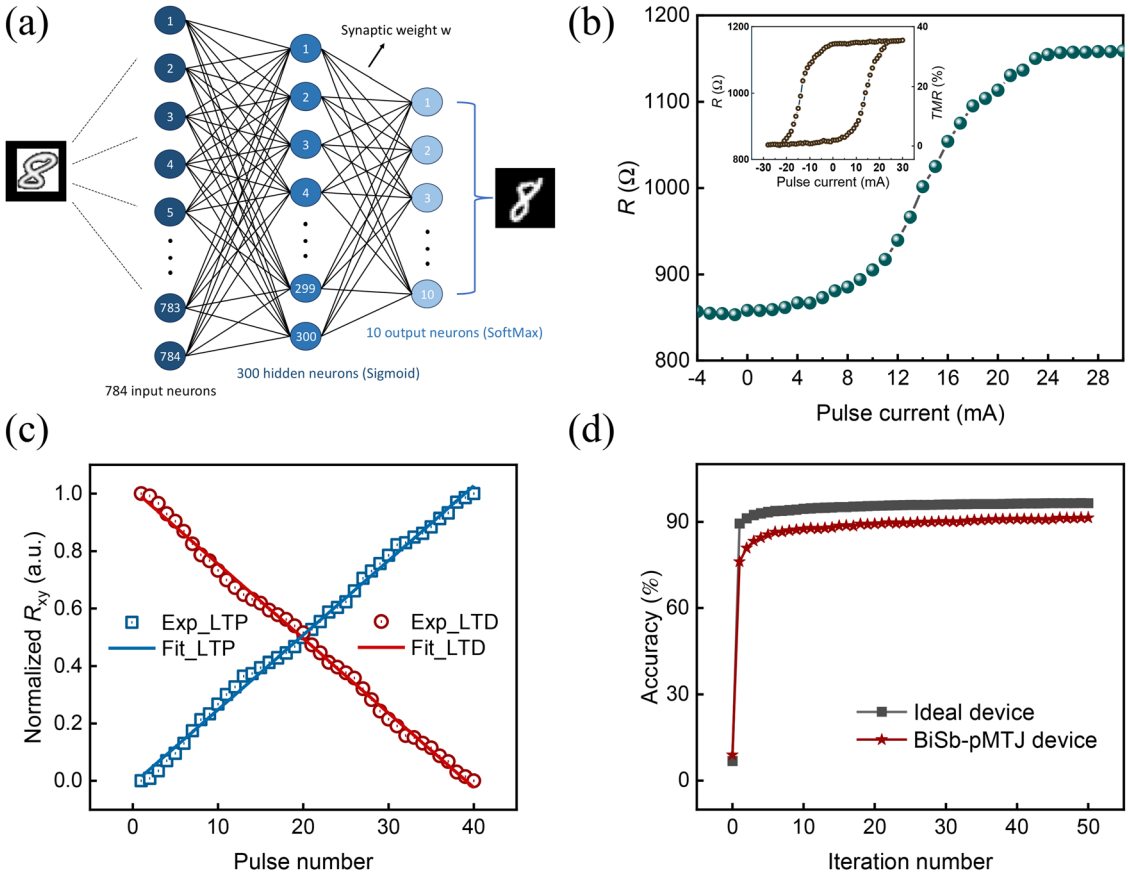

FIG. 4. (a) Schematic of the artificial neural network for pattern recognition, consisting of 784 input neurons, 300 hidden neurons, and 10 output neurons. Nodes represent neurons, and connections represent synapses with synaptic weights. (b) The resistance (R) in the BiSb-pMTJ as a function of pulse current amplitude exhibits an S-shaped nonlinear relationship, demonstrating its use as neurons with sigmoid activation functions. The inset shows the full loop of current-induced magnetization switching in the device. The measurement was performed on a device with a diameter of 10 μm. (c) Demonstration of long-term potentiation (LTP) and long-term depression (LTD) in the synaptic device. Experimental data (Exp_LTP and Exp_LTD) and corresponding fitting curves (Fit_LTP and Fit_LTD) are presented. (d) Evolution of pattern recognition accuracy for digit identification based on the resistance values in the synaptic devices. The plot compares the performance of the ideal synaptic device with the BiSb-pMTJ device.

a Ta buffer layer, we achieved a threefold enhancement in damping-like SOT efficiency and a 60% reduction in switching current compared to control samples. XRD analysis confirmed improved crystalline quality with increasing BiSb thickness, contributing to the enhanced spin current generation. Additionally, BiSb-pMTJs were shown to emulate key neuromorphic functionalities, including long-term potentiation/depression and sigmoidal activation behavior. When applied in a neural network for digit recognition, the devices achieved over 90% accuracy, validating their suitability for in-memory computing. This work highlights sputtered BiSb as a scalable, high-efficiency spin source for next-generation spintronic devices, enabling unified memory and neuromorphic computing functions.

See supplementary material for details on the AFM roughness analysis, magnetic anisotropy evaluation, XRD spectra, Ta buffer effect, TMR reproducibility, and switching behavior in BiSb-pMTJ devices.

This work was supported by the MOE Tier 1 (Grant No. RG76/23).

AUTHOR DECLARATIONS

Conflict of Interest

The authors have no conflicts to disclose.

Author Contributions

S. Wu: Data curation (equal); Investigation (equal); Methodology (equal); Validation (equal); Writing – original draft (equal); Writing – review & editing (equal). **G. J. Lim:** Methodology (equal); Validation (equal); Writing – review & editing (equal). **F. N. Tan:** Methodology (equal); Validation (equal); Writing – review & editing (equal). **T. L. Jin:** Methodology (equal); Validation (equal); Writing – review & editing (equal). **C. C I. Ang:** Formal analysis (equal); Validation (equal); Writing – review & editing (equal). **E. K. Koh:** Data curation (equal); Investigation (equal); Software (equal). **S. H. Lee:** Formal analysis (equal); Methodology (equal). **K. J. Cheng:** Investigation (equal); Validation (equal). **W. S. Lew:** Conceptualization (equal); Formal analysis (equal); Project administration (equal); Supervision (equal); Writing – review & editing (equal).

DATA AVAILABILITY

The data that support the findings of this study are available from the corresponding author upon reasonable request.

REFERENCES

[1]D. Apalkov, B. Dieny, and J. M. Slaughter, "Magnetoresistive random access memory," Proc. IEEE **104**(10), 1796–1830 (2016).
[2]M. Julliere, "Tunneling between ferromagnetic films," Phys. Lett. A **54**(3), 225–226 (1975).
[3]T. Miyazaki and N. Tezuka, "Giant magnetic tunneling effect in Fe/Al_2O_3/Fe junction," J. Magn. Magn. Mater. **139**(3), L231–L234 (1995).
[4]J. S. Moodera, L. R. Kinder, T. M. Wong, and R. Meservey, "Large magnetoresistance at room temperature in ferromagnetic thin film tunnel junctions," Phys. Rev. Lett. **74**(16), 3273–3276 (1995).
[5]W. H. Butler, X.-G. Zhang, T. C. Schulthess, and J. M. MacLaren, "Spin-dependent tunneling conductance of Fe| MgO| Fe sandwiches," Phys. Rev. B **63**(5), 54416 (2001).
[6]D. C. Ralph and M. D. Stiles, "Spin transfer torques," J. Magn. Magn. Mater. **320**(7), 1190–1216 (2008).
[7]L. Liu, C.-F. Pai, Y. Li, H. W. Tseng, D. C. Ralph, and R. A. Buhrman, "Spin-torque switching with the giant spin Hall effect of tantalum," Science **336**(6081), 555–558 (2012).
[8]G. Yu, P. Upadhyaya, Y. Fan, J. G. Alzate, W. Jiang, K. L. Wong, S. Takei, S. A. Bender, L.-T. Chang, Y. Jiang, M. Lang, J. Tang, Y. Wang, Y. Tserkovnyak, P. K. Amiri, and K. L. Wang, "Switching of perpendicular magnetization by spin–orbit torques in the absence of external magnetic fields," Nat. Nanotechnol. **9**(7), 548–554 (2014).
[9]S. Wu, T. L. Jin, F. N. Tan, C. C. I. Ang, H. Y. Poh, G. J. Lim, and W. S. Lew, "Enhancement of spin–orbit torque in Pt/Co/HfOx heterostructures with voltage-controlled oxygen ion migration," Appl. Phys. Lett. **122**(12), 122403 (2023).
[10]J. Ryu, S. Lee, K.-J. Lee, and B.-G. Park, "Current-induced spin–orbit torques for spintronic applications," Adv. Mater. **32**(35), 1907148 (2020).
[11]W. J. Kong, C. H. Wan, C. Y. Guo, C. Fang, B. S. Tao, X. Wang, and X. F. Han, "All-electrical manipulation of magnetization in magnetic tunnel junction via spin–orbit torque," Appl. Phys. Lett. **116**(16), 162401 (2020).
[12]S. Z. Rahaman, I.-J. Wang, D.-Y. Wang, C.-F. Pai, Y.-C. Hsin, S.-Y. Yang, H.-H. Lee, Y.-J. Chang, Y.-C. Kuo, Y.-H. Su, G.-L. Chen, F.-M. Chen, J.-H. Wei, T.-H. Hou, S.-S. Sheu, C.-I. Wu, and D.-L. Deng, "Size-dependent switching properties of spin-orbit torque MRAM with manufacturing-friendly 8-inch wafer-level uniformity," IEEE J. Electron Devices Soc. **8**, 163–169 (2020).
[13]N. Sato, F. Xue, R. M. White, C. Bi, and S. X. Wang, "Two-terminal spin–orbit torque magnetoresistive random access memory," Nat. Electron. **1**(9), 508–511 (2018).
[14]Y. Fan, P. Upadhyaya, X. Kou, M. Lang, S. Takei, Z. Wang, J. Tang, L. He, L.-T. Chang, M. Montazeri, G. Yu, W. Jiang, T. Nie, R. N. Schwartz, Y. Tserkovnyak, and K. L. Wang, "Magnetization switching through giant spin–orbit torque in a magnetically doped topological insulator heterostructure," Nat. Mater. **13**(7), 699–704 (2014).
[15]X. Che, Q. Pan, B. Vareskic, J. Zou, L. Pan, P. Zhang, G. Yin, H. Wu, Q. Shao, P. Deng, and K. L. Wang, "Strongly surface state carrier-dependent spin–orbit torque in magnetic topological insulators," Adv. Mater. **32**(16), 1907661 (2020).
[16]J. Han, A. Richardella, S. A. Siddiqui, J. Finley, N. Samarth, and L. Liu, "Room-temperature spin-orbit torque switching induced by a topological insulator," Phys. Rev. Lett. **119**(7), 77702 (2017).
[17]H. Wu, A. Chen, P. Zhang, H. He, J. Nance, C. Guo, J. Sasaki, T. Shirokura, P. N. Hai, B. Fang, S. A. Razavi, K. Wong, Y. Wen, Y. Ma, G. Yu, G. P. Carman, X. Han, X. Zhang, and K. L. Wang, "Magnetic memory driven by topological insulators," Nat. Commun. **12**(1), 6251 (2021).
[18]P. Li, W. Wu, Y. Wen, C. Zhang, J. Zhang, S. Zhang, Z. Yu, S. A. Yang, A. Manchon, and X. Zhang, "Spin-momentum locking and spin-orbit torques in magnetic nano-heterojunctions composed of Weyl semimetal WTe2," Nat. Commun. **9**(1), 3990 (2018).
[19]Y. Wang, D. Zhu, Y. Wu, Y. Yang, J. Yu, R. Ramaswamy, R. Mishra, S. Shi, M. Elyasi, K.-L. Teo, Y. Wu, and H. Yang, "Room temperature magnetization switching in topological insulator-ferromagnet heterostructures by spin-orbit torques," Nat. Commun. **8**(1), 1364 (2017).
[20]H. Wu, P. Zhang, P. Deng, Q. Lan, Q. Pan, S. A. Razavi, X. Che, L. Huang, B. Dai, K. Wong, X. Han, and K. L. Wang, "Room-temperature spin-orbit torque from topological surface states," Phys. Rev. Lett. **123**(20), 207205 (2019).
[21]N. H. D. Khang, Y. Ueda, and P. N. Hai, "A conductive topological insulator with large spin Hall effect for ultralow power spin–orbit torque switching," Nat. Mater. **17**(9), 808–813 (2018).
[22]B. Cui, A. Chen, X. Zhang, B. Fang, Z. Zeng, P. Zhang, J. Zhang, W. He, G. Yu, P. Yan, X. Han, K. L. Wang, X. Zhang, and H. Wu, "Low-power and field-free perpendicular magnetic memory driven by topological insulators," Adv. Mater. **35**(31), 2302350 (2023).
[23]T. Fan, N. H. D. Khang, S. Nakano, and P. N. Hai, "Ultrahigh efficient spin orbit torque magnetization switching in fully sputtered topological insulator and ferromagnet multilayers," Sci. Rep. **12**(1), 2998 (2022).
[24]T. Fan, N. H. D. Khang, T. Shirokura, H. H. Huy, and P. N. Hai, "Low power spin–orbit torque switching in sputtered BiSb topological insulator/perpendicularly magnetized CoPt/MgO multilayers on oxidized Si substrate," Appl. Phys. Lett. **119**(8), 82403 (2021).
[25]C.-F. Pai, "Switching by topological insulators," Nat. Mater. **17**(9), 755–757 (2018).

[26]V. Kateel, V. Krizakova, S. Rao, K. Cai, M. Gupta, M. G. Monteiro, F. Yasin, B. Sorée, J. De Boeck, S. Couet, P. Gambardella, G. S. Kar, and K. Garello, "Field-free spin–orbit torque driven switching of perpendicular magnetic tunnel junction through bending current," Nano Lett. **23**(12), 5482–5489 (2023).
[27]S. Wu, G. J. Lim, F. N. Tan, T. L. Jin, C. C. I. Ang, K. J. Cheng, and W. S. Lew, "Voltage-modulated magnetic properties and enhanced thermal endurance in Ta/Mo-based perpendicular magnetic tunnel junctions," J. Magn. Magn. Mater. **629**, 173293 (2025).
[28]S. Wu, T. Jin, C. C. I. Ang, G. J. Lim, B. W. H. Cheng, Ze. Chen, and W. S. Lew, "Electric field control of spin-orbit torque in annealed Ta/CoFeB/HfO x heterostructures via interfacial oxidation modulation," Nanotechnology **35**(36), 365205 (2024).
[29]L. Liu, D. Wang, D. Wang, Y. Sun, H. Lin, X. Gong, Y. Zhang, R. Tang, Z. Mai, Z. Hou, Y. Yang, P. Li, L. Wang, Q. Luo, L. Li, G. Xing, and M. Liu, "Domain wall magnetic tunnel junction-based artificial synapses and neurons for all-spin neuromorphic hardware," Nat. Commun. **15**(1), 4534 (2024).
[30]W. Cai, Y. Huang, X. Zhang, S. Wang, Y. Pan, J. Yin, K. Shi, and W. Zhao, "Spintronics intelligent devices," Sci. China Phys., Mech. Astron. **66**(11), 117503 (2023).
[31]J. Grollier, D. Querlioz, K. Y. Camsari, K. Everschor-Sitte, S. Fukami, and M. D. Stiles, "Neuromorphic spintronics," Nat. Electron. **3**(7), 360–370 (2020).
[32]Y. Zhang, Z. Zhang, K. Lin, Z. Zheng, X. Feng, and W. Zhao, in *2023 IEEE Nanotechnology Materials and Devices Conference* (IEEE, 2023), pp. 208–209.
[33]T. Jin, B. Zhang, F. Tan, G. J. Lim, Z. Chen, J. Cao, and W. S. Lew, "Granular magnetization switching in Pt/Co/Ti structure with HfOx insertion for in-memory computing applications," Nano Lett. **24**(18), 5521–5528 (2024).
[34]B. Zhang, W. Lv, Y. Guo, B. Wang, K. Luo, W. Li, and J. Cao, "Realization of multi-level state and artificial synapses function in stacked (Ta/CoFeB/MgO)N structures," Adv. Electron. Mater. **9**(2), 2200939 (2023).
[35]M. Hayashi, J. Kim, M. Yamanouchi, and H. Ohno, "Quantitative characterization of the spin-orbit torque using harmonic Hall voltage measurements," Phys. Rev. B **89**(14), 144425 (2014).
[36]J. Sasaki, S. Namba, S. Takahashi, Y. Hirayama, and P. N. Hai, "Highly efficient spin current source using BiSb topological insulator/NiO bilayers," Jpn. J. Appl. Phys. **62**(SC), SC1005 (2023).
[37]S. Bandiera, R. C. Sousa, Y. Dahmane, C. Ducruet, C. Portemont, V. Baltz, S. Auffret, I. L. Prejbeanu, and B. Dieny, "Comparison of synthetic antiferromagnets and hard ferromagnets as reference layer in magnetic tunnel junctions with perpendicular magnetic anisotropy," IEEE Magn. Lett. **1**, 3000204 (2010).
[38]E. K. Koh, P. A. Dananjaya, L. Liu, C. X. X. Lee, G. J. Lim, Y. S. You, and W. S. Lew, "Leveraging tunability of localized-interfacial memristors for efficient handling of complex neural networks," ACS Nano **18**(43), 29602–29617 (2024).
[39]K. Cai, T. Jin, and W. S. Lew, "Spin-based magnetic random-access memory for high-performance computing," Natl. Sci. Rev. **11**(3), nwad272 (2024).